We are IntechOpen,
the world's leading publisher of
Open Access books
Built by scientists, for scientists

4,800
Open access books available

122,000
International authors and editors

135M
Downloads

Our authors are among the

154
Countries delivered to

TOP 1%
most cited scientists

12.2%
Contributors from top 500 universities

BOOK CITATION INDEX
CLARIVATE ANALYTICS
INDEXED

WEB OF SCIENCE™

Selection of our books indexed in the Book Citation Index
in Web of Science™ Core Collection (BKCI)

Interested in publishing with us?
Contact book.department@intechopen.com

Numbers displayed above are based on latest data collected.
For more information visit www.intechopen.com

Effect of Argon Carrier Gas Flux on TiO$_2$ Nanostructures

Reza Sabet Dariani and Zohreh Nafari Qaleh

Additional information is available at the end of the chapter

Abstract

TiO$_2$ nanowires (NWs) have been fabricated by thermal evaporation method, using the vapor–liquid–solid (VLS) growth method and Au thin layer as a catalyst which were coated on titanium/quartz substrate. Optical and microstructure properties of TiO$_2$ NWs have been reviewed under different argon carrier gas flows. The gas flow was varied from 60 to 170 sccm. The X-ray diffraction patterns showed that TiO$_2$ NWs formed in rutile phase and their preferred orientation was in (110). The field emission scanning electron microscope figures indicated that with increasing gas flow, nanowires became thinner and longer. The absorbance curve of TiO$_2$ nanowires has been drawn by using spectrophotometer and their band gap was measured. Our results showed that the band gap has been enhanced in comparison with bulk one due to the quantum confinement. Also, the band gap enhanced from 3.35 to 3.45 eV by increasing the argon flow, since the wires became thinner and longer. The Williamson–Hall mechanism was applied as the vital tools for characterization of crystallite size and microstrain. Also, microstructure properties have been studied by X-ray diffraction analysis such as; dislocation density and texture coefficient. The crystallinity of TiO$_2$ NWs has been made better by enhancing Ar flow due to increasing of VLS growth method.

Keywords: TiO2, Nanostructure, Absorption coefficient

1. Introduction

1.1. Semiconducting nanowires

Based on the geometry, 1D nanostructures typically consist of four categories: nanowire (NW), nanorod (NR), nanobelt (NB), and nanotube. The first three categories all possess a solid structure, while the nanotube has a hollow center. There is a significant different in geometry, property, and synthesis strategies between the nanotube and the first three categories, i.e., NW, NR, and NB. In general, NRs are NWs with a small aspect ratio (i.e., short NWs), which

typically appear rigid and straight. NB is a special NW structure with a rectangular cross-section. Typical NB structures are single crystals with well-defined side crystal facets. Sometimes, nanofibers were also used to describe the NW morphology, particularly when the NWs are very long and not single crystalline [1]. Nanoscaled materials are of great interest for their unique structure and properties. Compared to isotropic nanoparticles and two dimensional thin films, one dimensional nanostructures such as nanofibers and nanowires are much more anisotropic, i.e., the aspect ratio of length to diameter can attain very high values.

Semiconductor one-dimensional structures, i.e., nanorods and nanowires with diameters ranging from 1 to 400 nm and lengths of up to hundreds of micrometers, are known to have many interesting physical properties and great potential applications in semiconductor and electronic technologies, which have stimulated intensive, worldwide research activities. They are perhaps the most versatile building blocks for optical and (opto-)electronic circuits at the nanoscale. Preliminary studies of some of these one-dimensional nanostructures indicate that they may be used as microscopic probes, field emission sources, storage materials, and light-emitting devices with extremely low power consumption. Among these semiconductors, some metal oxides, for instance, stannic oxide, titanium oxide, cuprous oxide, and vanadium pentoxide are the most important base materials in industry for gas sensors, transistors, and electrode material as well as catalysts. There has been extensive research into various "top-down" and "bottom-up" methods to create these nanostructures. In order to investigate their properties, many methods have been developed to synthesize one-dimensional nanomaterials, such as carbon nanotubes confined chemical reaction, Chemical Vapor Deposition (CVD), Molecular Beam Epitaxy (MBE), vapor-liquid-solid (VLS), solution–liquid–solid (SLS), and template-based synthetic approaches. However, complicated apparatus, complex process control, and special condition may be required for these approaches [2, 3]. Here we will describe VLS method in details.

**1.2. Titanium dioxide (TiO$_2$)**

Based on the geometry, 1D nanostructures typically consist of four categories: nanowire (NW), nanorod (NR), nanobelt (NB), and nanotube. The first three categories all possess a solid structure, while the nanotube has a hollow center. There is a significant difference in geometry, property, and synthesis strategies between the nanotube and the first three types, i.e., NW, NR, and NB. Generally, NRs are NWs with a small aspect ratio (short NWs), which typically become rigid and straight. NB is a special NW structure with a rectangular cross- section. Typical NB structures are single crystals with well-defined side crystal facets. Sometimes, nanofibers were also used to explain the NW morphology, particularly when the NWs are very long and not single crystalline.

Since Fujishima and Honda (1972) reported that n-type titanium dioxide (TiO$_2$) could be used as a photo anode for a photo electrochemical cell, titanium oxide has been comprehensively investigated owing to its great applications in many fields [4].

TiO$_2$ naturally exhibits four different types of polymorphs, i.e., rutile, anatase, brookite, and TiO$_2$ (B). In addition, several metastable polymorphs, such as TiO$_2$ (H), TiO$_2$ II, and perovskite, have been produced synthetically. Different phases have different properties and thus require

different conditions to form desired morphologies and offer different performance. In general, rutile is the most stable phase, while the anatase, brookite, and TiO$_2$ (B) are metastable and will transform into rutile under high temperature. This phase stability relationship also exists in TiO$_2$ nanomaterial formations. Anatase phased nanomaterials were commonly obtained but always found in solution-based or low-temperature vapor deposition systems. High- temperature deposition or annealing would usually yield rutile TiO$_2$ nanostructures. Brookite and TiO$_2$ (B) phases were less common and typically obtained from solution-based growth systems. Other metastable phases have to be synthesized using particular types of precursors and under restrict conditions. They were very rarely observed as a stable nanomaterial phase [1, 5, 6].

Indeed among the semiconductor oxides, titanium oxide (TiO$_2$) has received more attention during the last decade because of its high refractive index (2.5), high band gap (3 eV), transparency throughout the visible and infrared region, high chemical stability, and hardness [7]. Crystal structures of the two most important phases are anatase (a = 3.78 Å, c = 9.51 Å; space group of I4$_1$/amd) and rutile (a = 4.59, c = 2.96, space group of P4$_2$/mnm). Each cell of rutile consists of two TiO$_2$ molecules, while anatase has four TiO2 molecules. Figure 1 gives crystal structures of rutile (a) and anatase (b). The common features for these structures are as follows: Ti atom is positioned at the center of six O atoms, forming a deformed Ti-O octahedron. The octahedral share top points and a rhombic side join together and thus construct a crystal. The differences between them exist: three sides shared for the brookite, four for anatase and two for rutile. Among them rutile is the most stable and anatase is less while brookite is not stable. Therefore, the first two are commonly concerned in nanomaterials [4].
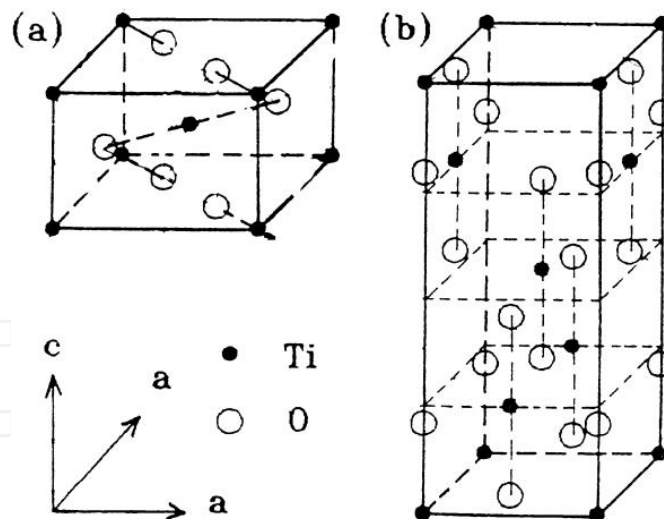
**Figure 1.** Two kinds of TiO$_2$ crystal structures: (a) rutile, (b) anatase.

TiO$_2$ has showed a wide range of applications in hydrogen production, lithium-ion batteries, fuel cells, gas sensors, detoxification, photovoltaics, photocatalysts, and super capacitors due to its excellent solid-state physical properties [8]. Over the past two decades, there have been remarkable advances in the expansion of one-dimensional (1D) nanostructures. The wire-like structure not only introduces significant enlarged and well-defined crystal surfaces over

planar structures but also provides 1D confined channel, which could basically tailor the transportation of electrons, phonons, and photons [9]. The one-dimensional structure such as TiO_2 nanowire is considered as a good candidate for getting higher performance in those applications compared to the bulk one. For example, a TiO_2 nanowire based electrode can provide a large surface area for effectively collecting photons and electrons [8]. Tao et al. [10] used TiO_2 NW array as photo anodes of back-illuminated dye-sensitized solar cells. Shi et al. [11] grew TiO_2 nanorods uniformly on dense Si NW array backbones, by using surface-reaction-limited pulsed chemical vapor deposition technique. They developed a 3D high-density heterogeneous NW architecture, which is useful for photo electrochemical electrodes. Wang et al. [12] reported hydrogen-treated TiO_2 NW arrays for photo electrochemical water splitting. Mandal and Bhattacharyya [13] presented through systematic studies the performance of TiO_2 NWs in sensing, quantification, and photocatalytic degradation of cationic dyes in aqueous solution. Wang et al. [14] indicated that TiO_2 NWs have promising application for high energy density lithium-ion batteries. Xi et al. [15] grew single-crystalline rutile TiO_2 nanorods on fluorine doped tin oxide glass for organic–inorganic hybrid solar cells by means of hydrothermal mechanisms.

Numerous routes have been explored to the synthesis of 1D TiO_2 nanostructures from both bottom up and top down. Representative bottom-up approaches include a large variety of solution- and vapor-based growth strategies. Although bottom-up approaches remain as the major synthesis efforts, several top-down procedures have also been explored for 1D TiO_2 growth, such as direct oxidation and electrochemical etching techniques. In general, there are four main approaches, which include solution-based synthetic approaches (such as hydro-thermal/ solvothermal and sol-gel methods), vapor-based approaches (chemical/physical vapor deposition, atomic layer deposition-related methods and pulsed laser deposition), templated growth, and top-down fabrication techniques. Solution-based growth techniques offer several major advantages for mass production of nanomaterials including low-cost, simple processing, and good scalability. Vapor deposition is typically conducted in vacuum and under high temperature. Compared to the wet chemistry methods, it offers several unique advantages. First, the high quality of NW's crystallinity is secured due to the utilization of high-temperature and high-vacuum deposition conditions. Second, since the vapor deposition processes are typically performed in conventional thin film deposition systems, the knowledge of thin film growth techniques can be adopted to understanding the NW growth behaviors. Lastly, by engineering catalysts, growth sites, or precursors, the control of location, composition, dimension, and organization of NWs could be achieved via vapor deposition processes. Nevertheless, vapor deposition is usually associated with high cost and small- scale production. Template growth is a very versatile synthesis technique that forms nanostructure with a morphology that follows the porous template. Top-down fabrication techniques describe the creation of nanostructures from the bulk form. This approach typically is able to process a large quantity of nanostructures with uniform morphology and orientation. For TiO_2 1D nanostructures, a top-down process usually starts from a bulk Ti foil followed by selective etching and/ or oxidization. In the following section, the vapor- liquid- solid mechanism is described [1].

1.3. VLS mechanism of nanowire growth

Nanowires are commonly grown using vapor, solution or (template directed) electrodeposition methods. High- temperature growth from the vapor phase is often preferred due to the high crystal quality that can be obtained and the ability to grow large quantities of wires at once. A key factor in most vapor- and solution-based methods is the presence of small metal droplets during synthesis. Analysis of the growth of silicon whiskers (hairs) from the vapor phase using gold catalyst particles leads to the postulation of the vapor- liquid- solid (VLS) mechanism of growth. The VLS mechanism consists of three stages which are illustrated in figure 2A. First, a metal particle absorbs semiconductor material and forms an alloy. In this step, the volume of the particle increases and the particle often transition from a solid to a liquid state. Second, the alloy particle absorbs more semiconductor material until it is saturated. The saturated alloy droplet becomes in equilibrium with the solid phase of the semiconductor and nucleation occurs (i.e., solute/solid phase transition). During the final phase, a steady state is formed in which a semiconductor crystal grows at the solid/liquid interface. The precipitated semiconductor material grows as a wire because it is energetically more favorable than extension of the solid- liquid interface. The semiconductor material is precipitated at the existing solid/liquid interface as opposed to the formation of a new interface.
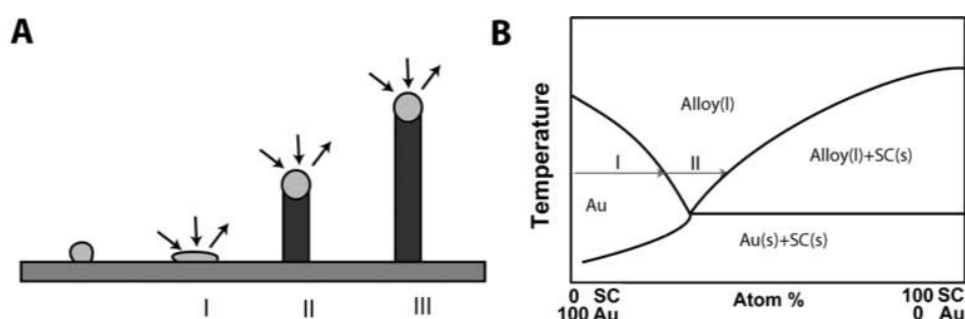
Figure 2. (A) The stages of (I) alloying, (II) nucleation, and (III) growth of nanowire synthesis according to the VLS growth mechanism. (B) Pseudobinary phase diagram of a semiconductor-gold system. The arrows indicate the subsequent phases when a gold droplet absorbs semiconductor material at a constant temperature. (1) At first, the gold particle is in the solid or liquid state. By absorbing semiconductor material, a liquid alloy is formed. (II) Subsequent absorption of more semiconductor material allows the liquid alloy to be in equilibrium with the solid semiconductor [2].

In the VLS mechanism, the wire diameter is determined by the diameter of the alloy particle which is in turn determined by the low temperature size of the metal particle and the temperature. The wire length is determined by the growth rate and time. When the system is cooled, the alloy droplet solidifies at the wire tip. To examine the feasibility of VLS wire growth from a certain semiconductor/metal combination, it is essential to study the (pseudo)binary phase diagram (figure 2B); the metal should form an alloy with the semiconductor at a temperature that also allows the semiconductor to exist in the solid phase. The validity of the VLS mechanism of wire growth has been proven for germanium nanowires by in- situ high- temperature TEM measurements. Heating neighboring gold and germanium clusters to growth temperatures and selectively evaporating the germanium clusters with an electron beam are allowed for the direct imaging of the successive steps of alloying and melting, nucleation and wire growth. A study using colloidal gold catalyst particles showed that using the VLS method,

(single) crystalline nanowires with diameters as small as 5 nm could be obtained. In addition, it has been shown that by increasing the VLS growth rate by modulating the temperature, crystallization only takes place at the surface of the catalyst particle resulting in the growth of nanotubes. Since the late 1990's, semiconductor nanowire growth using the VLS method has enjoyed an increasing popularity with researchers and industry [2].

Some of studies on TiO_2 nanowires are listed in Table 1.

Year	Researcher	Fabrication method	Carrier gas	References
2002	Zhang et al.	Hydrothermal synthesis	None	[16]
2003	Pradhan et al.	Metalorganic chemical vapor deposition	500–800 sccm (Ar)	[17]
2006	Lee et al.	VLS	100 sccm (Ar) + 0.5 sccm(O_2)	[18]
2006	Wu et al.	Thermal evaporation	20 sccm (Ar) + 1 sccm (O_2)	[19]
2006	Gyorgy et al.	Pulsed laser deposition	None	[20]
2007	Amin et al.	VLS	10 sccm (Ar)/ 10 sccm (Ar) + 1 sccm (O_2)	[21]
2007	Berger et al.	Chemical bath deposition	None	[22]
2008	Huo et al.	Thermal	150 sccm (Ar)	[23]
2008	Baik et al.	VLS	200 sccm (Ar)	[24]
2009	Huo et al.	Direct Growth on ti foil	50 sccm (Ar)	[25]
2011	RamezaniSani et al.	Thermal evaporation	50- 150 sccm (Ar)	[26]
2011	Liu et al.	water-assisted chemical vapor deposition	400 sccm (Ar)	[4]
2011	Park et al.	VLS and VS	200 sccm (Ar)	[27]
2011	Ha et al	VLS	Ar with 2% H_2 upon reaching 1 atm	[28]
2012	Wu et al.	Solvothermal method	None	[29]
2012	Shang et al.	Thermal Evaporation	100 sccm (Ar)	[30]
2013	Liu et al.	Low-temperature hydrothermal method.	None	[31]
2013	Dariani et al.	VLS	60- 170 sccm (Ar)	[32]
2013	Tian et al.	Electron beam lithography	None	[33]
2013	Liu et al	Molten-salt flux method	None	[34]
2014	Nechache et al.	Pulsed laser deposition	300 mTorr (O_2/Ar)	[35]
2015	Wang et al.	Confined-space synthesis at low temperature	None	[36]

Table 1. Some of works on the fabrication of TiO_2 nanowires

The vapor–liquid–solid and the vapor–solid growth mechanisms have been used to fabricate high-quality oxide NWs with short heating times. Ha et al. [28] synthesized single-crystalline rutile TiO$_2$ NWs by VLS method on Ti foil substrates patterned with catalytic Sn nano-islands, Lee et al. [18] grew TiO$_2$ NWs in this way but used Au as catalysts, and Park and Lee [27] reported synthesis of TiO$_2$ NWs by Ni as catalysts.

TiO$_2$ nanowire is typically achieved using either of the two different synthetic methods developed over the past few years: one is the wet-chemistry method such as electrochemical, sol-gel electrophoresis, hydrothermal growth on Ti substrates at 180 ℃ utilizing various organic solvents to oxidize Ti [37], direct oxidizing Ti substrate with aqueous hydrogen peroxide solutions [10], and solvothermal method [38]. The other is the dry method such as, growth single-crystalline TiO$_2$ nanowires by thermal evaporation in atmospheric-pressure (101325 Pa) [30], metal-organic chemical vapor deposition [39], pulsed chemical vapor deposition [8], chemical vapor transport process by evaporating Ti metal powders [18], heating titanium grids (substrate) by ethanol-embedding followed by an annealing in the air [40], and by a facile water- assisted chemical vapor deposition method based on commercial metal titanium [4]. TiO$_2$ nanowires produced by the wet-chemistry method due to poor crystallinity have difficulty integrating into device fabrication. Also, they need additional processes in order to improve their crystallinity [27].

In this work, TiO$_2$ nanowires were synthesized by a carbothermal evaporation process on quartz substrate at 850 ℃ for 1 h at atmospheric pressure (101325 Pa), and Au was used as a catalyst. Also, the influence of argon flow as carrier gas on microstructural and optical characteristics was measured. We have been characterized some microstructural parameters like crystallite size, microstrain within the crystallite, dislocation density, and texture coeffi-cient by the diffraction pattern.

2. Experimental details

In this study, pieces of quartz with dimensions of $1 \times 15 \times 15$ mm^3 are used. Initially, the substrates were ultrasonically cleaned with acetone and ethanol for 10 minutes, respectively. Then a layer of titanium was deposited on substrates by electron beam evaporation technique with the evaporation rate of 0.2 Å/s under the pressure of 1.5×10^{-5} mbar. In this step, voltage and current were kept 4 kV and 100 mA, respectively. The electron beam evaporation device is specified by: HIND HIGH VACUUM CO. Model 12A4D. After removing the samples, a gold thin layer with 3 nm thickness was coated on the titanium layer by sputtering method.

In next step, a tablet containing of titanium and graphite with the ratio of 1:1 as a source material was placed in the center of horizontal furnace. The center of the furnace was heated to 1050℃ with heating rate of 20℃/min. According to phase diagram of the Au-Ti system, the eutectoid temperature is about 832℃ [30]. The eutectoid temperature is a point in which two metals in solid phase form an alloy in solid phase (no in liquid phase). Thus, the sample was placed in distance of 12 - 13 cm (with about 850 ℃ temperature) from the center of the furnace for 1 h at atmospheric pressure and under argon flow. The vapor was generated from source
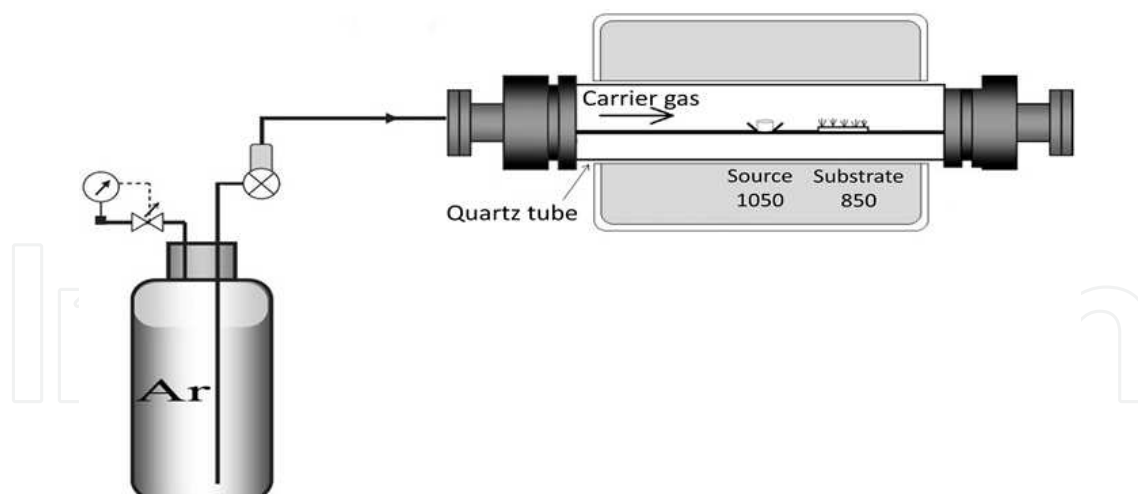
Figure 3. A schematic of CVD system.

material transported to the substrate and at last condensed on the surface of substrate (see figure 3). Then the substrate was naturally cooled down to room temperature. In this study, three samples under different argon gas flows (60 sccm, 110 sccm, and 170 sccm) were fabricated. Argon gas was also used to control the oxygen content of experiment. It is believed that oxygen comes from leaked air during heating process. Content of argon was kept constant during heating process by using bubbling trap at the end of the vent line. The microstructure and the morphology of the samples were analyzed by x-ray diffraction (XRD: Philips X-Pert PW 3040/60, λ (Cukα) = 1.54 $°$A) and field emission scanning electron microscope (FESEM: Hitachi S4160 with operating voltage of 15 kV), respectively. The absorption spectrum of TiO_2 nanostructures was evaluated by spectrophotometer (Ocean Optics, Model HR4000 CG-UV-NIR).

3. Results and discussion

3.1. SEM observations

The morphologic characteristics of the samples under different carrier gas flows are determined by SEM images. The cross-sectional views of the samples are shown in figure 4.

The average range of length and diameter of nanowires are given in Table 2. It can be seen that nanowires become thinner and longer with increasing the carrier gas flow. Since fabrication parameters except argon flow were fixed, it can be concluded that the amount of O_2 inside the reaction chamber plays a vital role in the growth of TiO_2 1D nanostructures. When the O_2 concentration was high, i.e., Ar flow was low, the VLS growth (will describe later) was suppressed because Ti vapor could readily react with O_2 before forming alloy droplets with Au as catalyst [12]. Therefore, in this condition, a relatively low concentration of O_2 is necessary [13].
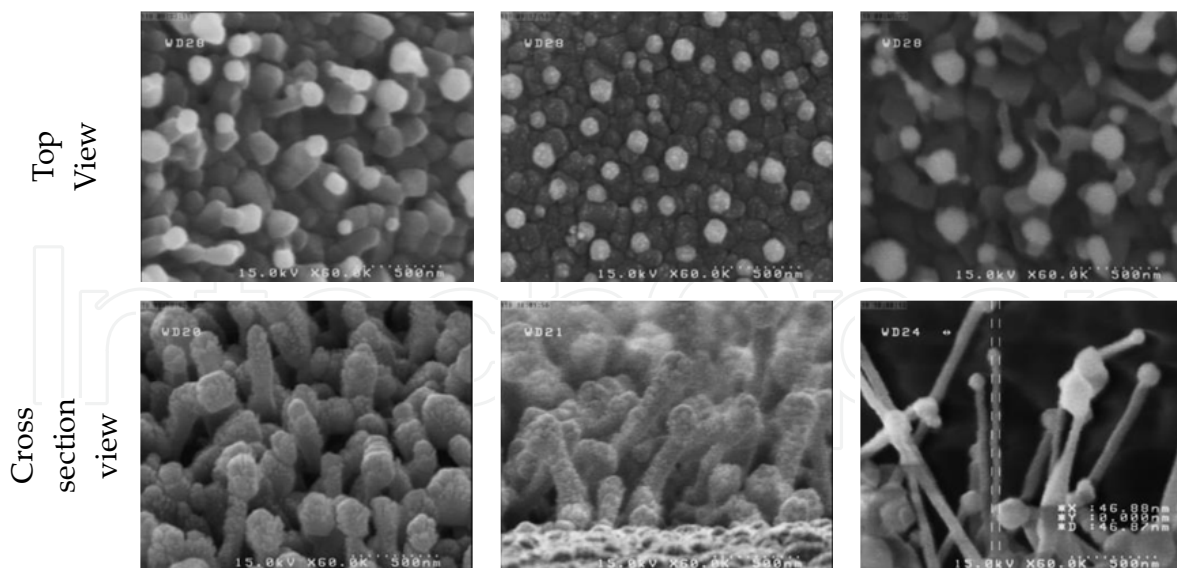
Figure 4. Top and cross-sectional SEM views of TiO$_2$ nanostructures. Argon gas flow increases from left to right.

Sample	Argon flow (sccm)	Average Diameter (nm)	Average Length (nm)
S1	60	121	390
S2	110	117	648
S3	170	72	1021

Table 2. Average values of diameter and length of nanowires.

Figure 5 shows compositional energy-dispersive X-ray spectroscopy (EDAX) analysis of the NW tip and the confirmation of the existence of Au alloy.
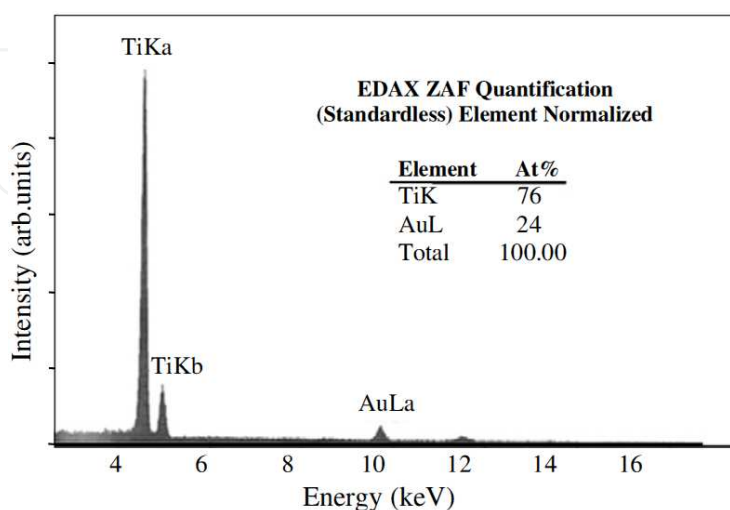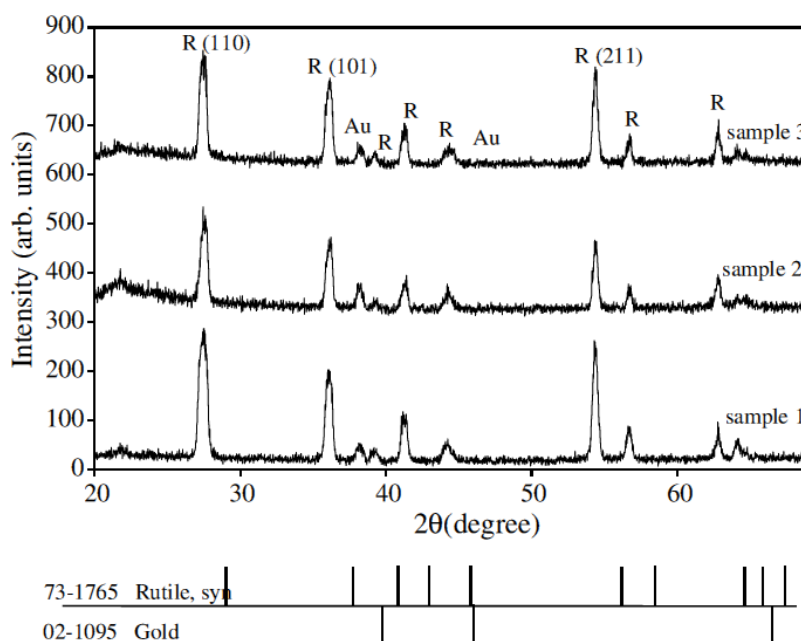

Figure 5. A typical EDAX of our samples which shows the existence of Au.

3.2. XRD studies

To examine the effect of argon flow on structural properties of TiO$_2$ 1D nanostructure, the XRD analyses were performed. Figure 6 shows XRD patterns of TiO$_2$ grown on Ti/quartz substrates.

Figure 6. XRD patterns of TiO$_2$ nanowires at different carrier gas flows.

Rutile phase is formed on the samples and (110) direction is preferred direction which is consistent with SEM images. In the TiO$_2$ tetragonal structure, the plane spacing (d) is related to lattice constants (a and c) and the Miller indices (h, k, and l) by the following relation [42]:

$$1 / \left(d_{hkl}\right)^2 = h^2 + k^2 / a^2 + l^2 / c^2 \tag{1}$$

The results are presented in Table 3 and are consistent with standard card of JCPDS (73-1765).

Sample	a (Å)	c (Å)	Eg (eV)
S1	4.586	2.951	3.35±0.02
S2	4.583	2.955	3.39±0.02
S3	4.589	2.949	3.45±0.02
JCPDS	4.589	2.954	

Table 3. Lattice constants and E g of nanowires at different carrier gas flows.

3.3. Optical properties

The absorbance spectrum of TiO$_2$ nanowires is measured by spectrophotometer. According to Beer-Lambert's law (Eq. 2), transmittance (Eq. 3), and absorbance (Eq. 4) definitions [43], the absorption coefficients of samples according to absorbance are obtained by Eq. 5:

$$I(\lambda) = I_0(\lambda)e^{-\alpha(\lambda)d} \tag{2}$$

$$T(\lambda) = I(\lambda)/I_0(\lambda) \tag{3}$$

$$A(\lambda) = -Log(T_\lambda) \tag{4}$$

$$\alpha = \left(-1/d\right)Ln\left(10^{-A}\right) = (A/d)Ln(10) \tag{5}$$

where d is the thickness of samples derived from the cross-sectional images of SEM and A is the absorbance of samples.

It is known that the relationship between absorption coefficient α near the absorption edge and the optical band gap E_g is determined by Tauc relation [15]:

$$\alpha h\nu = C\left(h\nu - E_g\right)^n \tag{6}$$

where C is a constant, n is equal to 0.5 or 2 for direct and indirect allowed transitions, respectively, and $h\nu$ is photon energy. The E_g can be graphically estimated by a linear fit of the high-energy tail of $(\alpha h\nu)^{1/n}$. Since the samples have rutile structure, rutile titania has direct band gap ($n = 0.5$).

Figure 7 shows $(\alpha h\nu)^2$ plots versus photon energy $h\nu$ for direct transition and intercepts value of the linear-fit extrapolations with the horizontal axes. The values of E_g are given in Table 2.

The optical results have shown that all the samples are characterized by energy gap higher than bulk rutile TiO$_2$ (E_g = 3 eV for bulk) [28]. As the carrier gas concentration increases, the band gap increases from 3.35 to 3.45 eV. The higher value of the rutile titania energy gap are attributable to the well-known relationship between band gap and crystallites size. The appearance of quantum confinement effect in small sized nano crystalline titania is resulting in a blue shift of the band gap [37]. Among the samples, sample 3 has the highest E_g value which is the thinnest one.
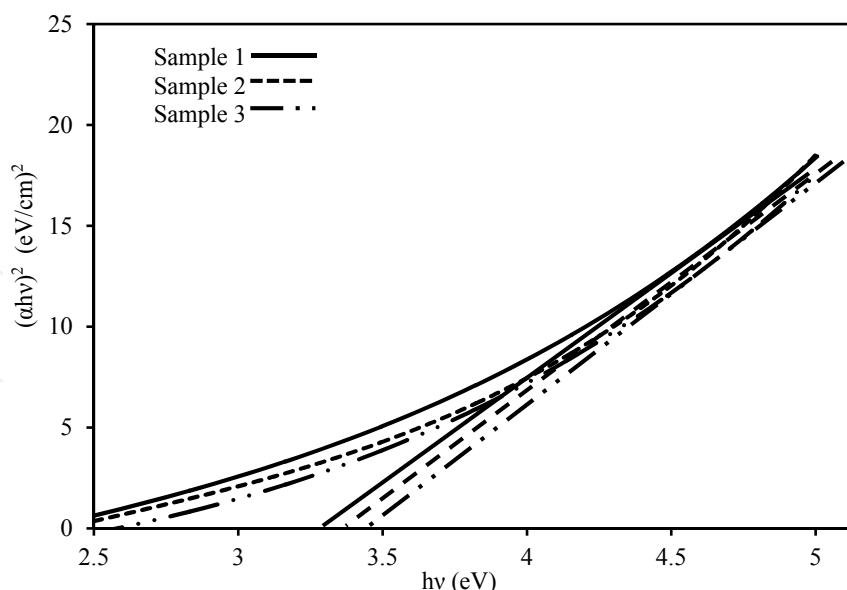
Figure 7. $(\alpha h\nu)^2$ curves versus photon energy ($h\nu$) for the samples.

3.4. Growth mechanism

One-dimensional nanostructures are grown in this study by VLS mechanism. In the mechanism, the role of the impurity (catalyst) is to form a liquid alloy droplet of eutectoid temperature. Metal catalyst used in the mechanism was gold with 3 nm thickness. At high temperatures (about 850℃) alloy liquid droplets of Au-titanium form. On the other hand, during the thermal evaporation process, at first, titanium powder in the presence of oxygen atmosphere was converted toTiO$_2$ powder (see Eq. 7) [44], then the TiO$_2$ powder was reduced by graphite to produce Ti vapor as the following chemical reaction [45].

$$Ti(s)+O_2(g)=TiO_2(s) \quad (298\text{-}2500 \quad) \tag{7}$$

$$TiO_2(s)+C(s)=Ti(g)+CO_2(g) \tag{8}$$
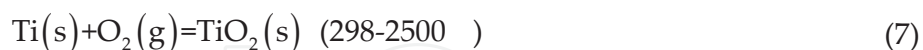
We have used Ti metal and carbon instead of TiO$_2$ in carbothermal reduction process. In fact, Ti in the tablet converts to TiO$_2$ by oxygen in air (Eq. 7), and then TiO$_2$ is reduced in carbothermal reduction process by carbon (Eq. 8). Indeed, carbon mainly was used for TiO$_2$ reduction. Also there are some papers that have used titanium and carbon as a source material [26, 46]. Previously, TiO$_2$ and C as a source material were examined in our lab but NWs did not grow. Amin et al. [21] also reported that continuous increase of the amount of oxygen further reduced the yield of TiO$_2$ 1D nanostructures. When the O$_2$ concentration was high, the VLS growth was suppressed because Ti vapor could readily react with O$_2$ before forming alloy droplets with catalytic materials.

Since the adsorption of liquid is more than solid, the reactant components (vapor of titanium and oxygen) absorbed into the alloy. The liquid alloy acts as a preferred sink for arriving nanostructure components. The Ti and O$_2$ are dissolved into the mediating alloy liquid droplets. When alloy droplets reach to saturation of reactive component, the 1D nanostructures grow by precipitation of TiO$_2$ from the droplets in the interface liquid- solid to minimize free energy of alloy system. The 1D nanostructure grows in length by the mechanism until the Au is consumed or until the growth conditions are changed [47]. Here, by over an hour, furnace temperature began to reduce and growth condition of one-dimensional titanium dioxide nanostructures is stopped.

Usually droplets of catalyst are observed on the top of the nanostructures in a VLS- based growth system. However, the position of catalyst at the tip or root of the nanostructure depends on the interaction of catalyst nanoparticles and the substrate [48].

SEM images (Figure 4) show by increasing argon flow or decreasing oxygen (one of reactants), nanowires become thinner and longer. O$_2$ plays a main role in the growth of TiO$_2$ nanowires. When O$_2$ concentration is high, i.e., Ar flow is low, Ti vapor could readily react with O$_2$, before they adsorb on alloy droplets [30]. Therefore, in this condition, a relatively low concentration of O$_2$ is necessary [15, 31]. According to other findings [17, 27, 48], we suggest that thinner and longer NWs with increasing Ar flow are due to the following reasons:
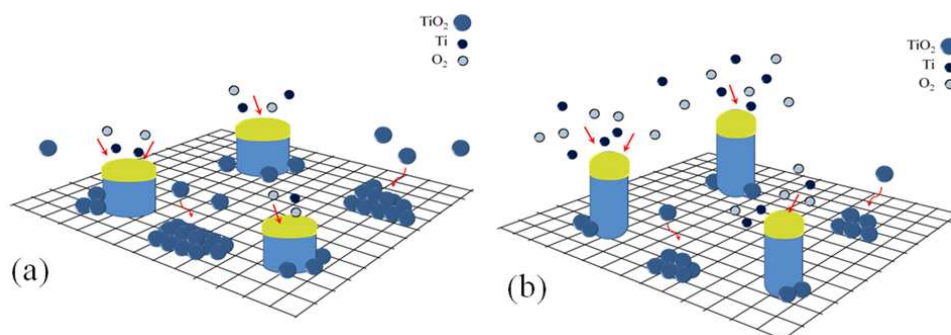
Figure 8. Schematic illustration of growth procedure for TiO$_2$ nanowires on Ti/quartz substrate in (a) low and (b) high argon carrier gas flow [32].

Argon flux plays a major role in combining Ti and O$_2$ and producing TiO$_2$. A schematic of the proposed growth mechanism is shown in Figure 8. When Ar flux is low (Figure 8a), the possibility of producing TiO$_2$ is much higher than when Ar flux is high (Figure 8b). The reason could be due to moving Ti and O$_2$ gases from furnace tube when Ar flux is high and so the possibility of producing TiO$_2$ becomes lower. On the other hand, in presence of O$_2$, titanium layer on the substrate surface in 850℃ is easily converted to TiO$_2$ (according to XRD diffraction patterns and Eq. 7). Thus, there is a competitive growth between TiO$_2$ layer (epitaxial growth: TiO$_2$ molecules on TiO$_2$ layer) and alloy droplets (VLS growth). TiO$_2$ islands that are formed around the NWs by VLS method become larger with decreasing Ar flow. Since the other parameters of growth, such as source and time are constant, NW diameters and lengths become larger and shorter, respectively.

Moreover, TiO_2 is heavier than Ti and O_2, so probably exists in lower height than them. Therefore, TiO_2 can be absorbed into the nanostructure bodies more likely than their tips (alloy droplets), to be absorbed, so when TiO_2 is more than Ti and O_2, nanostructures will be shorter and thicker. Therefore, with increasing Ar gas flow, the crystallinity improves due to VLS growth method.

RamezaniSani et al. [26] have grown TiO_2 nanowires by thermal evaporation on a silicon substrate with the major reflection along (101) direction. Their results indicate that a convenient gas flow for controlling diameter size of nanowires is about 100 sccm, While our substrate is quartz and the major reflection growth along is (110) direction. Also we see that with increasing gas flow from 60 to 170 sccm, nanowires become thinner and longer.

3.5. Microstructure characterization (theoretical background)

Deviation from the ideal crystallinity such as finite crystallite size, strain (at the atomic level), and extended defects (stacking faults and dislocations) leads to broadening of the diffraction lines. Crystallite size is a measure of the size of coherently diffracting domains and is not generally the same as particle size due to polycrystalline aggregates. Strain is defined as change in length per unit length and is measured as the change in d spacing of a strained sample compared to the unstrained state [49].

According to Scherrer [50], the apparent crystallite size can be obtained as follows:

$$D_V = \left(K\lambda / \text{ FWHM} \right) cos\theta \tag{9}$$

where K is a constant close to unity, θ is the Bragg angle of the (*hkl*) reflection, and λ is the wavelength of X-rays used. D_V is a volume-weighted quantity. Wilson in 1963 used integral breadth β instead of FWHM in Eq. (9).

The dependence of strain ε to line broadening is defined as follows [51]:

$$\varepsilon = \left(\beta / 4 \right) cot\theta = \beta / \left(4 tan\theta \right) \tag{10}$$

When the XRD patterns are adjusted to a combination of Cauchy and Gaussian line shapes, the Halder and Wagner approximation is better suited for obtaining the physical broadening [52]:

$$\beta_f \approx \left(\left(\beta_h \right)^2 - \left(\beta_g \right)^2 \right) / \beta_h \tag{11}$$

where β_g, β_h, and β_f refer to the integral breadths of the instrumental, observed, and measured (physical) profiles, respectively.

3.5.1. The Williamson–Hall integral breadth method

Williamson and Hall in 1953 proposed a method for resolving size and strain broadening. Williamson–Hall plots can be applied to a Gaussian profile as follows [53]:

$$\left(\beta_f^*\right)^2 = \left(\beta_f cos\theta\,/\,\lambda\right)^2 = \left(1\,/\left(D_v\right)^2\right) + 4\varepsilon^2 d^{*2} \tag{12}$$

A plot of $(\beta_f^{*2})^2$ against $4d^{*2}$ gives a straight line. From the intercept and slope of line size, strain can be calculated.

3.6. Microstructure study in TiO₂ nanowires

X-ray diffraction (XRD), in which strong scattered intensity is observed at specific angles of scattering, has been widely used for decades in the determination of structural and micro-structural parameters. By the diffraction pattern, we have characterized some microstructural parameters like crystallite size, microstrain within the grain, dislocation density, and texture coefficient.

3.7. The Williamson–Hall integral breadth method

From an analysis of XRD line broadening, the contributions due to crystallite size and lattice strain can be determined. Here, crystallite size and microstrain contributions are separated using the Williamson–Hall (W-H) method. Assuming contribution to the Bragg peak having both Lorentz and Gauss profile [54]:

$$\text{Lorentz fit}\ : \beta_h = \beta_f + \beta_g\beta cos\theta\,/\,\lambda = \ 1\,/\,D + \ 4\varepsilon sin\theta\,/\,\lambda \tag{13}$$

$$\text{Gauss fit}: \beta_h^{\ 2} = \beta_f^{\ 2} + \beta_g^{\ 2}\left(\beta cos\theta\,/\,\lambda\right)^2 = \left(1\,/\,D\right)^2 + 16\varepsilon^2\left(sin\theta\,/\,\lambda\right)^2 \tag{14}$$

By plotting $\beta cos\theta/\lambda$ vs $sin\theta/\lambda$ (Lorentz) or $(\beta cos\theta/\lambda)^2$ vs $(sin\theta/\lambda)^2$ (Gauss), one can estimate the microstrain from the line slope and inverse of the crystallite size from its *y*-intercept. Figures 9 and 10 indicate W-H curves for the samples in Lorentz and Gauss fits, respectively. The obtained values from W-H curves are given in Table 4. The plotted W-H curves indicate that strain and size contributions exist simultaneously in the samples.

θ (%)	D (nm) (Guass)	D (nm) (Lorentz)	ε (%) (Guass)	ε (%) (Lorentz)	Sample
0.232	14.14±0.42	14.28±0.38	0.448±0.020	0.375±0.015	S1
0.228	15.58±0.53	15.16±0.52	0.359±0.012	0.251±0.008	S2
0.169	15.85±0.53	15.27±0.51	0.427±0.014	0.361±0.012	S3

Table 4. Crystallite size, mean microstrain, and dilatation values of the samples.
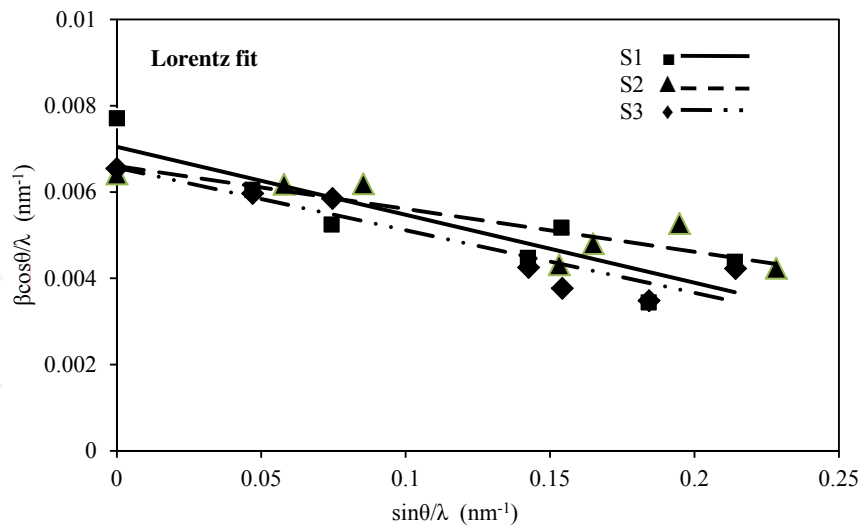
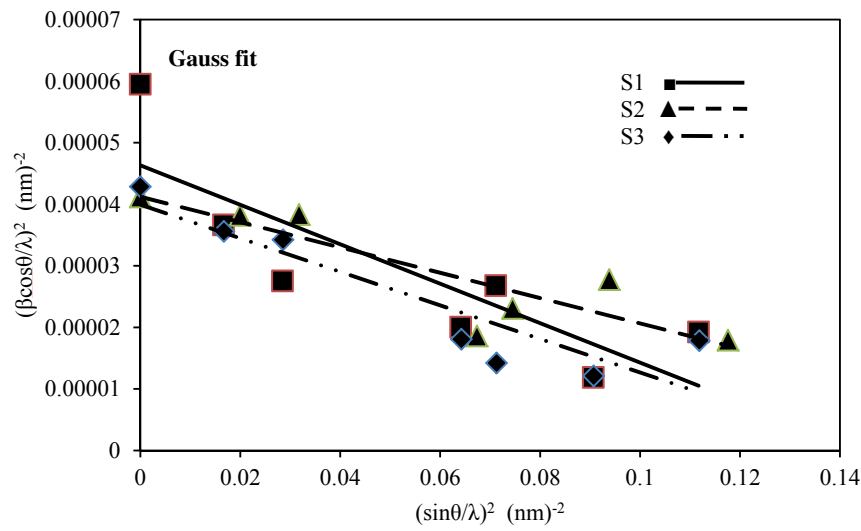**Figure 9.** Williamson-Hall curves for the samples: Lorentz fit.

Figure 10. Williamson-Hall curves for the samples: Gauss fit.

3.8. Dilatation

Volume strain or dilatation is a change in volume that defines as [55]:

$$\theta \equiv \Delta v / v \tag{15}$$

If three strain ε_{xx}, ε_{yy}, and ε_{zz} have been treated as small quantities, the dilatation is [55]

$$\theta = \partial \xi / \partial x + \partial \eta / \partial y + \partial \zeta / \partial z = \varepsilon_{xx} + \varepsilon_{yy} + \varepsilon_{zz} \tag{16}$$

The horizontal strain $\varepsilon_{\parallel}$ and vertical strain $\varepsilon_{\perp}$ are calculated by the expression as follows: $\varepsilon_{\parallel}=(a_{epi}-a_0)/a_0$ and $\varepsilon_{\perp}=(c_{epi}-c_0)/c_0$ [56], where a_0 and c_0 are the lattice constants of bulk TiO$_2$ (a_0= 4.587 Å, c_0= 2.954 Å [57]). Here $\varepsilon_{xx}=\varepsilon_{yy}=\varepsilon_{\parallel}$ and $\varepsilon_{zz}=\varepsilon_{\perp}$; thus, the dilatation becomes.

$$\theta = 2\varepsilon_{\parallel} + \varepsilon_{\perp} \tag{17}$$

The calculated dilatations are given in Table 4. The slopes of the W-H curve for the samples are negative, i.e., their strain is negative and there is a contraction of epilayer on substrates which means compressive stress. The different slopes represent different mean microstrains.

It is well known that strain has direct relation with elastic energy [55]. Evaporated particles from source due to their temperature have certain kinetic energy. In low Ar flow (60 sccm), Ar particles is lower than evaporated particles then collision between them is negligible. However, with increasing Ar flow to 110 sccm, collision between Ar particles and evaporated particles increases therefore it could have reduced the evaporated particles energies and microstrain. However, with increasing Ar flow up to 170 sccm, the number of Ar particles enhanced compared to evaporated particles, so they can help to increase the evaporated particles movement. Therefore, their velocity and energy increase and also mircostrain increases.

Both dilatation and microsrain are negative and at the same order. We compare these two quantities, because the microstrain (obtained from W-H curve) is average of strain in volume not in specific direction. Thus, calculated strain from main definition must consider in volume.

We can compare volume strain (which found from lattice parameters) and microstrain (which found from XRD pattern) because the microstrain from the W-H curve does not have any particular direction. By comparing them, it reveals that they have approximately good agreement both in magnitude and sign.

3.9. Dislocation density

To estimate the dislocation density, ρ_D (dislocation density due to domain size), ρ_ε (dislocation density due to strain) and ρ (real dislocation density), the simple approach of Williamson and Smallman (1956) is followed, relating ρ to crystallite size D and strain $<\varepsilon^2>^{1/2}$ [58]:

$$\rho_D = 3 / D^2 \tag{18}$$

$$\rho_\varepsilon = 4 < \varepsilon^2 > /b^2 \tag{19}$$

$$\rho = \left(\rho_D \cdot \rho_\varepsilon\right)^{1/2} = 2\sqrt{3} < \varepsilon^2 >^{1/2} /\left(bD\right) \tag{20}$$

where b is the Burger's vector, which determines distance and direction of displacement. We assumed that the magnitude of Burger's vector is calculated by $[(a^2/4)+(a^2/4)+(c^2/4)]^{1/2}$, where a and c are lattice parameters. Dislocation densities in actual crystals depend on the preparation of the specimen, but can range from 10^2 to 10^{12} cm^{-2} [59], and the dislocation values of our samples are in the same range (Table 5).

According to Eq. 16, behavior of dislocation density is similar to microstrain, i.e., the value of dislocation density decreases from sample S1 to S2, 4and then increases from S2 to S3, since dislocation density and microstrain are related to displacement. It is noted that the results of Lorentz and Gauss fits for our samples are the same.

ϱ (cm^{-2}) × 10^{11} - Lorentz	ρ (cm^{-2}) × 10^{11}- gauss	b (Å)	Sample
2.55	3.08	3.563	S1
1.61	2.24	3.562	S2
2.30	2.62	3.564	S3

Table 5. Burger's vectors and dislocation densities of the samples.

3.10. Texture coefficient

In order to clearly understand the preferred orientation of the samples, the texture coefficient TC(hkl) of each XRD pattern is calculated according to the following formula [60]:

$$TC(hkl) = \left[I(hkl)/I_0(hkl) \right] / (1/N)\Sigma_N I(hkl)/I_0(hkl) \tag{21}$$

where $I(hkl)$ is measured intensity of the (hkl) diffraction peak and N is the amount of crystal directions which is 11, 10, and 12 for samples 1, 2, and 3, respectively. If TC(hkl) equals to 1, there is no preferred orientation on (hkl) direction of the film. When this value is larger than 1, a preferred orientation exists along the (hkl) plane. The standard deviation TC(hkl) of the TC values from powder condition is [60]:

$$\sigma = \left[(1/N)\Sigma_N \left\{ TC(hkl) \right\}^2 - 1 \right]^{1/2} \tag{22}$$

If σ equals to zero, the crystallite orientation of a film sample is the same as that of the related powder-shaped sample and there is no preferred direction. Therefore, σ value indicates the preferred orientation level of thin film samples [61]. The values of texture coefficient and its standard deviation for the samples are shown in Table 6. As expected, the preferred direction in the samples is (110). It is concluded that the different carrier gas flows do not influence the preferential orientation. The rutile (110) surface is the most stable crystal face and has lowest surface energy [62].

According to Table 6, the behavior of TC (110) is similar to dislocation density, i.e., dislocation helps the growth of (110) plane, which is the most stable plane in the rutile phase.

TC(110)/∑TC(hkl)	σ	TC (211)	TC (101)	TC (110)	Sample
38.9	0.68	2.32	1.81	2.63	S1
38.5	0.53	1.69	1.89	2.24	S2
35.3	0.68	2.32	2.25	2.49	S3

Table 6. Texture coefficient and its standard deviation for the samples.

In order to better determine the contribution of TC (110) to other TC (*hkl*), the proportion of its value to total value of all TC(*hkl*) was calculated, (i.e., TC(110)/∑TC(*hkl*)). The values obtained for samples 1, 2 and, 3 were 38.9, 38.5, and 35.3, respectively. It is observed that by increasing argon flow, the value of TC(110)/∑TC(*hkl*) is decreased. Since in the case of argon with 60 sccm flow, epitaxial growth has occurred more than the others, so it can make possible growth in the (110) plane, which is the most stable one in rutile TiO$_2$. However, in further argon flow, the epitaxial growth becomes lower which causes the reduction of TC (110).

4. Conclusion

In this study, single-crystalline rutile TiO$_2$ nanowires were fabricated under different argon gas flows. The results indicated that TiO$_2$ nanowires form in rutile phase and their preferred growth is in the (110) direction, since (110) plane in rutile phase has lowest surface energy. The band gap energy of TiO$_2$ nanowires have increased due to the quantum confinement compared with bulk one. The wires become thinner and longer by increasing the argon flow. In 170 sccm, which has the least amount of oxygen, the average value of diameter and the length of TiO$_2$ were respectively 72 and 1020 nm. The band gap of TiO$_2$ nanowires has increased from 3.35 to 3.45 eV and their crystallinity has improved by increasing argon flux due to enhancement of VLS growth mechanism.

The advantage of our method is to fabricate TiO$_2$ nanostructures without contamination and impurities. These materials can be used for photovoltaic and gas sensor applications due to their large surface to volume ratio.

Author details

Reza Sabet Dariani[*] and Zohreh Nafari Qaleh

*Address all correspondence to: dariani@alzahra.ac.ir

Department of Physics, Alzahra University, Tehran, Iran

References

[1] X. Wang, Z. Li, J. Shi, and Y. Yu, One-Dimensional Titanium Dioxide Nanomaterials: Nanowires, Nanorods, and Nanobelts, American Chemical Society, 2014, 114(19), p. 9346-9384.

[2] L. Karel van Vugt. Optical Properties of Semiconducting Nanowires. PhD thesis. Utrecht University; 2007.

[3] Z. Lin Wang. Nanowires and nanobelts materials, properties and devices. Volume 2: nanowires and nanobelts of Functional materials, Springer; 2006.

[4] H. Liu, Y. Zhang, R. Li, M. Cai, and X. Sun, J. Nanopart. Res. 13 (2011) 385-391.

[5] Y. Bai, I. Mora-Sero´, F. De Angelis, J. Bisquert, and P. Wang, Titanium Dioxide Nanomaterials for Photovoltaic Applications, American Chemical Society, 2014, 114(19), p.10095-10130.

[6] L. Liu and X. Chen, Titanium Dioxide Nanomaterials: Self-Structural Modifications, American Chemical Society, 2014, 114(19), p. 9890-9918.

[7] L. V. Saraf, S. I. Patil and S. B. Ogale. Synthesis of nanophase TiO_2 by ion beam sputtering and cold condensation technique. Int. J. Mod. Phys. B. 12, (1998) 2635-2647.

[8] J. Shi, X. Wang, J. Cryst. Growth 11 (2011) 949-954.

[9] J. Shi, C. Sun, M.B. Starr, and X. Wang, Nano Lett. 11 (2011), 624-631.

[10] R. Tao, J. Wu, H. Xue, X. Song, Xu Pan, X. Q. Fang, X.D. Fang, S.Y. Dai, J. Power Sources 195 (2010) 2989-2995.

[11] J. Shi, Y. Hara, C. Sun, M.A. Anderson, X. Wang, Nano Lett. 11 (2011) 3413-3419.

[12] G. Wang, H. Wang, Y. Ling, Y. Tang, X. Yang, R. C. Fitzmorris, C. Wang, J.Z. Zhang, and Y. Li, Nano Lett. 11 (2011) 3026-3033.

[13] S.S. Mandal, and A.J. Bhattacharyya, Talanta 82 (2010) 876-884.

[14] Y. Wang, M. Wu, and W.F. Zhang, Electrochim. Acta 53 (2008) 7863-7868.

[15] G.K. Mor, O.K. Varghese, M. Paulose, K. Shankar, C.A. Grimes, Sol. Energy Mater. Sol. Cells 90 (2006) 2011-2075.

[16] Y.X. Zhang,G.H. Li, Y.X. Jin,Y. Zhang, J. Zhang, L.D. Zhang, Chem. Phys. Lett. 2002; 365:300e4.

[17] S.K. Pradhan, P.J. Reucroft, F. Yang, and A. Dozier, J. Cryst. Growth 256 (2003) 83-88.

[18] J. Lee, K. Park, T. Kim, H. Choi and Y. Sung, Nanotechnology 17 (2006) 4317-4321.

[19] J.M. Wu, H. C. Shih, and W.T. Wu, Formation and photoluminescence of single-crystalline rutile TiO 2 nanowires synthesized by thermal evaporation, Nanotechnology 17 (2006) 105–109.

[20] E. György, et al., Growth of Au–TiO₂ nanocomposite thin films by a dual-laser, dual-target system, J. Appl. Phys. 100, 114302. 2006.

[21] S.S. Amin, A.W. Nicholls, and T.T. Xu., Nanotechnology 18 (2007) 445609-445609.

[22] T. Berger, T. Lana-Villarreal, D. Monllor-Satoca, R. Go´mez, The electrochemistry of transparent quantum size rutile nanowire thin films prepared by one-step low temperature chemical bath deposition, Chem. Phys. Lett. 447 (2007) 91–95.

[23] K. Huo, X. Zhang, L. Hu, X. Sun, J. Fu, et al., One-step growth and field emission properties of quasialigned TiO₂ nanowire/carbon nanocone core-shell nanostructure arrays on Ti substrates, Appl. Phys. Lett. 93 (2008) p. 013105.

[24] Jeong Min Baik, et al, High-yield TiO2 nanowire synthesis and single nanowire field-effect transistor fabrication, Appl. Phys. Lett. 92 (2008) 242111.

[25] K. Huo, et al., Synthesis and Field Emission Properties of Rutile TiO₂ Nanowires Arrays Grown Directly on a Ti Metal Self-Source Substrate, J. Nanosci. Nanotechnol, (2009) 3341–3346.

[26] S. RamezaniSani, A. Morteza Ali and R. Jafari, Physica E 43 (2011) 1809–1812.

[27] Y.S. Park, and J.S. Lee, Bull. Korean Chem. Soc. 32 (2011) 3571-3574.

[28] J.Y. Ha, B.D. Sosnowchik, L. Lin, D.H. Kang and A.V. Davydov, Appl. Phys. Express 4 (2011) 065002-065004.

[29] H.B. Wu, H.H. Hng, and X.W. Lou, Direct Synthesis of Anatase TiO₂ Nanowires with Enhanced Photocatalytic Activity, Adv. Mater., 24, 2567-2571, 2012.

[30] Z.G. Shang, Z.Q. Liu, P.J. Shang, J.K. Shang, J. Mater. Sci. Technol. 28 (2012) 385-390.

[31] J. Liu, Z. Liu, K. Lin, and A. Wei, Synthesis of Sub-10 Nm TiO₂ Nanowires For The Application of Dye-Sensitized Solar Cells, Func. Mater. Lett, 6, No. 2 (2013) 1350017.

[32] R.S. Dariani, Z. Nafari Qaleh, Microstructure characterization of TiO₂ nanowires fabricated by thermal evaporation process, Thin Solid Films 542 (2013) 192.

[33] W.C. Tian, Yu-Hsuan Ho, Chao-Hao Chen and Chun-Yen Kuo, Sensing Performance of Precisely Ordered TiO₂ Nanowire Gas Sensors Fabricated by Electron-Beam Lithography, Sensors 2013, 13, 865-874.

[34] B. Liu, et al., Large-Scale Synthesis of Transition-Metal-Doped TiO₂ Nanowires with Controllable Over potential, American Chemical Society, 135, 9995-9998, 2013.

[35] R. Nechache, M. Nicklaus, N. Diffalah, A. Ruediger and F. Rosei, Pulsed laser deposition growth of rutile TiO_2 nanowires on Silicon substrates, Appl. Surf. Sci. 313 (2014) 48–52.

[36] X. Wang, et al., Confined-space synthesis of single crystal TiO_2 nanowires in atmospheric vessel at low temperature: a generalized approach, Sci. Rep. 5 (2015) 8129.

[37] A. Hu, X. Zhang, K.D. Oakes, P. Peng, Y.N. Zhou, M.R. Servos, J. Hazard. Mater. 189 (2011) 278-285.

[38] Z. Wei, Y. Yao, T. Huang, A. Yu, Int. J. Electrochem. Sci. 6 (2011) 1871-1879.

[39] J.J. Wu, C.C. Yu, J. Phys. Chem. B 108 (2004) 3377-3379.

[40] Y. Huang, Y. Lee, V. Yeh, C. Cheng, J. Lumin. 129 (2009) 1762-1766.

[41] W. Luo, Z. Jin, H. Liu, and T. Wang, Calphad, 25 (2001) 19-26.

[42] Y. Waseda, E. Matsubara, and K. Shinoda, X-Ray Diffraction Crystallography: Introduction, Examples and Solved Problems, Springer-Verlag, Berlin, 2011.

[43] R.J.D. TILLEY, Colour and the Optical Properties of Materials, second ed., John Wiley & Sons Ltd, West Sussex, 2011.

[44] D.R. Gaskell, Introduction to the Thermodynamics of Materials, fourth ed., Taylor & Francis Publication, New York, 2009.

[45] F. Habashi, Handbook of Extractive Metallurgy, Vol II, Wiley publication, Weinheim, 1998.

[46] J.M. Wu, H.C. Shih, W.T. Wu, Y.K. Tseng, and I.C. Chen, Journal of Crystal Growth, 281 (2005) 384–390.

[47] R.S. Wagner, W.C. Ellis, Appl. Phys. Lett. 4 (1964) 89-90.

[48] M. NorouziBanis, Y. Zhang, R. Li, X. Sun, X. Jiang, and D. Nikanpour, Particuology 9(2011) 458-464.

[49] P. Pourghahramani, E. Forssberg. Microstructure characterization of mechanically activated hematite using XRD line broadening. Int. J. Miner. Process. 79 (2006) 106–11

[50] Scherrer, P., 1918. Bestimmung der Grösse und der inneren Structure von Kollooidteilchen mittels Röntgenstrahlung. Nachr. Ges. Wiss. Gött. 2, 98–100.

[51] Stokes, A.R., Wilson, A.J.C., 1944. The diffraction of X-rays by distorted crystal aggregates I. Proc. Phys. Soc. Lond. 56, 174.

[52] N.C. Halder, C.N.J. Wagner, 1966. Separation of particle size and lattice strain in integral breadth measurements. Acta Crystallogr. 20, 312–313.

[53] K. Santra, P. Chatterjee, S.P. Sen Gupta, 2002. Voigt modeling of size–strain analysis: application to α-Al$_2$O$_3$ prepared by combustion technique. Bull. Mater. Sci. 25 (3), 251–257.

[54] R. Guinebretiere, X-ray Diffraction by Polycrystalline Materials, Antony Rowe Ltd, Chippenham, 2007.

[55] W.C. Elmore and M.A. Heald, Physics of Waves, McGraw-Hill Book Company, USA, 1969.

[56] J. Xiong, J. Tang, T. Liang, Y. Wang, C. Xue, W. Shi, and W. Zhang, Appl. Surf. Sci. 257 (2010) 1161-1165.

[57] J. Muscat, V. Swamy, and N.M. Harrison, Phys. Rev. B 65(22) (2002) 224112-224112.

[58] P. Pourghahramani, E. Forssberg, Int. J. Miner. Process. 79 (2006) 120-139.

[59] N.W. Ashcroft, N.D. Mermin, Solid State Physics, Harcourt College Publishing, Fort Worth, 1976.

[60] K.H. Kim and J.S. Chun, Thin Solid Films 141 (1986) 287-295.

[61] L. Feng, J. Zhang, B. Li, W. Cai, Y. Cai, L. Wu, W. Li, J. Zheng, Q. Yan, G. Xia, and D. Cai, Thin Solid Films 491 (2005) 104-109.

[62] U. Diebold, Surf. Sci. Rep. 48 (2003) 53-229.